



Article

Mitigation Conducted Emission Strategy Based on Transfer Function from a DC-Fed Wireless Charging System for Electric Vehicles

Li Zhai ^{1,2,*} , Yu Cao ^{1,2} , Liwen Lin ^{1,2}, Tao Zhang ^{1,2} and Steven Kavuma ^{1,2}

¹ National Engineering Laboratory for Electric Vehicles, Beijing Institute of Technology, Beijing 100081, China; caoyu5501@163.com (Y.C.); 15201430735@163.com (L.L.); zhangtaohorizon@163.com (T.Z.); stevenkavuma@hotmail.com (S.K.)

² Collaborative Innovation Center of Electric Vehicles in Beijing, Beijing Institute of Technology, Beijing 100081, China

* Correspondence: zhaili26@bit.edu.cn; Tel.: +86-10-6891-5202

Received: 5 February 2018; Accepted: 20 February 2018; Published: 25 February 2018

Abstract: The large dv/dt and di/dt outputs of power devices in wireless charging system (WCS) in electric vehicles (EVs) always introduce conducted electromagnetic interference (EMI) emissions. This paper proposes a mitigation conducted emission strategy based on transfer function from a direct current fed (DC-fed) WCS for EVs. A complete test for the DC-fed WCS is set up to measure the conducted emission of DC power cables in a frequency range of 150 kHz–108 MHz. An equivalent circuit with high-frequency parasitic parameters for WCS for EV is built based on measurement results to obtain the characteristics of conducted emission from WCS. The transfer functions of differential mode (DM) interference and common mode (CM) interference were established. A judgment method of using transfer functions to determine the dominated interference mode responsible for EMI is proposed. From the comparison of simulation results between CM or DM and CM+DM interference, it can be seen that the CM interference is the dominated interference mode which causes the conducted EMI in WCS in EVs. A strategy of giving priority to the dominated interference mode is proposed for designing the CM interference filter. Finally, the conducted voltage experiment is performed to verify the mitigation conducted emission strategy. The conducted voltage of simulation and experiment is decreased respectively by 21.17 and 21.4 dB μ V at resonance frequency 30 MHz. The conducted voltage at frequency range of 150 kHz–108 MHz can be mitigated to below the limit level-3 of CISPR25 standard (GB/T 18655-2010) by adding the CM interference filters.

Keywords: electric vehicle; wireless charging system; conducted emission; mitigation strategy

1. Introduction

Wireless charging technologies, as an attractive alternative to cabled charging, are attracting widespread interest in the field of consumer electronics, medical implants and electric vehicles [1–4], due to their convenient and safe characteristics [5–7]. There are two kinds of power supply system in wireless charging system (WCS): alternating current fed (AC-fed) and direct current fed (DC-fed) system. DC-fed WCS is used in fast charging with high current and voltage and widely applied in electric vehicles (EVs) in future.

As for wireless charging for EVs, many researchers pay attention to improving the charging efficiency and electromagnetic compatibility (EMC). Some researchers adopt the method of optimizing the structure of the coupled coil pair, the compensation circuit and pulse width modulation (PWM) control strategy to improve the efficiency of wireless charging [8–13]. As for EMC, the two key considerations consist of electromagnetic emission and electromagnetic susceptibility (EMS).

The electromagnetic emission of WCS mainly includes the emission of the electromagnetic field (EMF) generated by the coupling coils, the conducted emission and the radiated emission from the power cables.

As for electromagnetic emission for WCS, there are lots of research mainly focused on reducing the EMF which will exposure to humans. Different power levels of WCS have been researched to analyze the distribution characteristics of EMF. Some kinds of method were proposed to reduce magnetic field exposure, including adding a shield plate, optimizing coils shape and ferrite arrangement, matching impedance and adding a reverse magnetic field [14–17]. The fast switching of these power semiconductor devices such as MOSFET used in inverter of WCS is controlled by PWM, as result in generation of conducted EMI and low power quality. In addition some radiated EMI due to conducted-EMI may be generated to influence or even damage some onboard components such as sensors, analog devices, wireless devices of EVs, etc. Therefore, it is very significant to predict and suppress the conducted-EMI for WCS.

However, few research on conducted-EMI for WCS was presented previously. Although some studies on the conducted-EMI from high-voltage systems in EVs such as motor drive system, DC–DC converter and onboard charger have been carried out [18–23], the model and characteristics of the conducted-EMI for WCS are not yet proposed. In addition, filtering is usually used to mitigate the conducted-EMI. The analysis and design method of EMI filtering are always proposed based on constant source impedance and load impedance which are varied in practice. It may lead to inadequate mitigation and generation of new resonance due to impedance mismatch. In addition, the common mode (CM) and DM filters are designed separately by CM and DM interference propagation respectively. Then a combination of the CM and DM filters can result in bulky volume and high cost, and induce an unwanted resonance due to parameters of filter and high frequency parasitic parameters. On the other hand, the DM interference can lead to the CM interference, and the CM interference also can lead to the DM interference. The DM filter or CM filter can mitigate both of the CM and DM interference simultaneously. Therefore, a combination of the CM and DM filters cause filtering repeatedly, it means over design.

From the above proposed problems, firstly, it is necessary to build an equivalent circuit with high-frequency parasitic parameters for WCS for EV to predict the conducted-EMI for WCS. From which the practical EMI source impedance and load impedance can be taken into consideration. Secondly, the transfer functions of DM interference and CM interference were established to predict and determine the dominated interference mode responsible for EMI from WCS in EVs. Meanwhile, comparison of simulation results between CM or DM and CM+DM interference is performed to prove dominated interference mode. Then, a strategy of giving priority to the dominated interference mode is proposed for designing filter.

The organization of this paper is as follows. Section 2 shows a complete test for the DC-fed WCS, in order to measure the conducted-EMI of DC power cables in a frequency range of 150 kHz–108 MHz. In Section 3, modeling and simulation of the WCS for the conducted-EMI are presented. In Section 4, analysis and estimation for the conducted-EMI is performed based on the transfer function, and a judgment method of using transfer functions to determine the dominated interference mode responsible for EMI is proposed. Section 5 gives the method of designing the filters. In Section 6, the conducted voltage experiment for WCS is performed to verify efficiency and feasibility of the mitigation conducted-EMI strategy. In Section 7, conclusions and future works are proposed.

2. System Conducted-EMI Emission Measurement

2.1. Conducted-EMI Emission Setup

A complete test setup for conducted-EMI emissions from a DC-fed WCS on an EV in an EMI laboratory as shown in Figure 1 and mainly consists of a DC voltage source, DC power cables, standard line impedance stabilization networks (LISNs), a wireless charging controller, a couple of coils and an

EMI-receiver. Measurements are performed to comply with the CISPR 25 standard which provides conducted EMI emission limits for vehicle components in a frequency range of 150 kHz to 108 MHz as shown in Table 1. Two LISNs terminated with 50 Ω resistances provide DC power from a DC voltage source to the wireless charging controller using two shielded cables (2 m). The power inverter in a wireless charging controller with 425 V DC input is connected to coupling coils using two shielded cables (1.5 m). The WCS operates at a frequency of 85 kHz with a working gap of 150 mm and a system transmission power of 3.7 kW with a circular magnetic coupler. With this configuration, the total conducted-EMI noise voltage signals in DC cables can be picked up by any one of LISNs impedances connected to an EMI receiver.

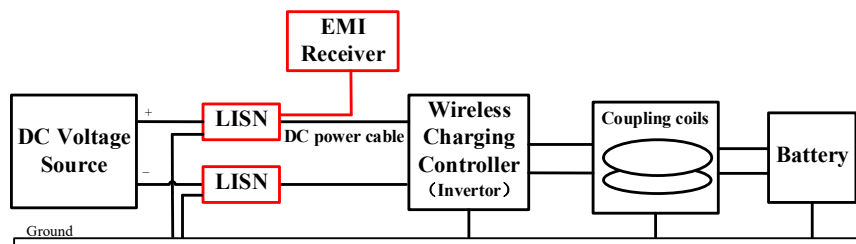


Figure 1. Conducted electromagnetic interference (EMI) emission system test setup for wireless charging system (WCS).

2.2. Conducted EMI Experiment Results

The test platform as shown in Figure 2 is set up. Figure 3 shows the experimental results and it can be found that the conducted-EMI noise voltage of the wireless charging controller is dominant in a frequency range of 150 kHz–108 MHz and is not compliant with CISPR25 (GB/T 18655), as shown in Table 1. From Figure 3, it can be seen that the conducted voltage exceeds the limit requirement in the range of 500 kHz–2 MHz and 30 MHz–108 MHz. Therefore, it is necessary to build a high frequency circuit mode for analyzing the source and paths of conducted-EMI so as to predict the conducted-EMI emissions.

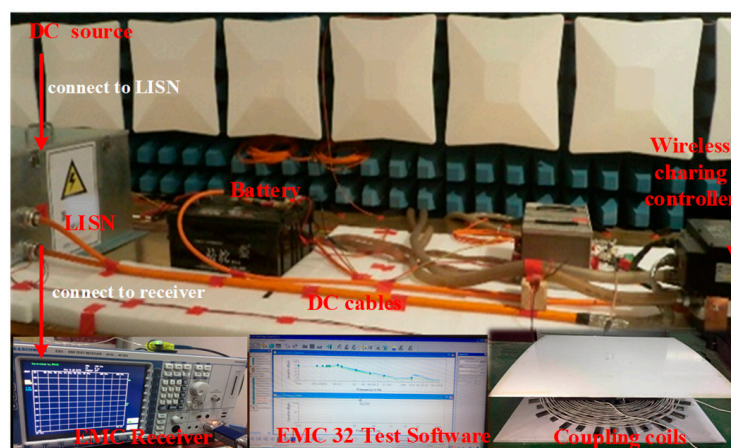


Figure 2. The test platform for conducted-EMI emission.

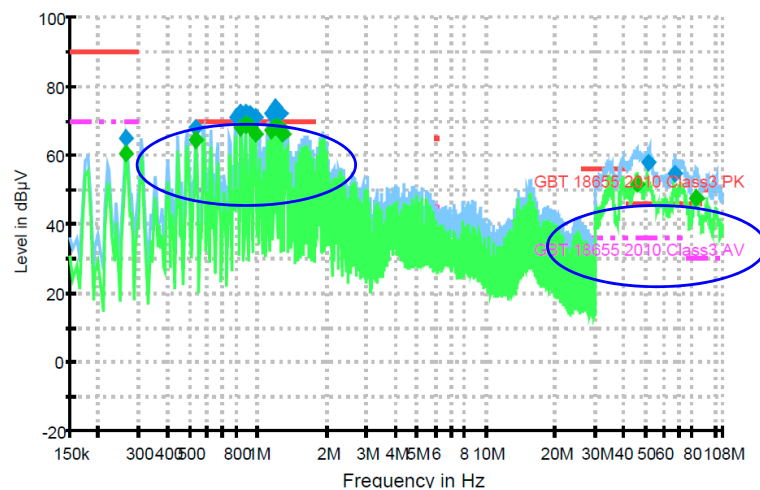


Figure 3. The measurement for conducted-EMI emission.

Table 1. CISPR25 class3-average limits for conducted voltage.

Frequency/MHz	Limit/dB (μ V)
0.15–0.30	70
0.53–1.8	50
5.9–6.2	45
26–28	36
30–88	36
88–108	30

3. System Modeling and Analysis

3.1. The Construction of WCS

Without any physical connection in WCS, the power of 425 V DC voltage at the ground side is transmitted to the vehicle side and converted into the power of the 400 V DC for the battery. The designed system mainly consists of DC voltage source V_{DC} , filter capacitor C_7 , full bridge inverter (S_1 – S_4), coupled coils (primary coil L_1 and secondary coil L_2), LCC compensation, rectification and filtering and electric vehicle battery V_{bat} can be seen in Figure 4. The circuit parameters of WCS are designed and calculated, as shown in Table 2.

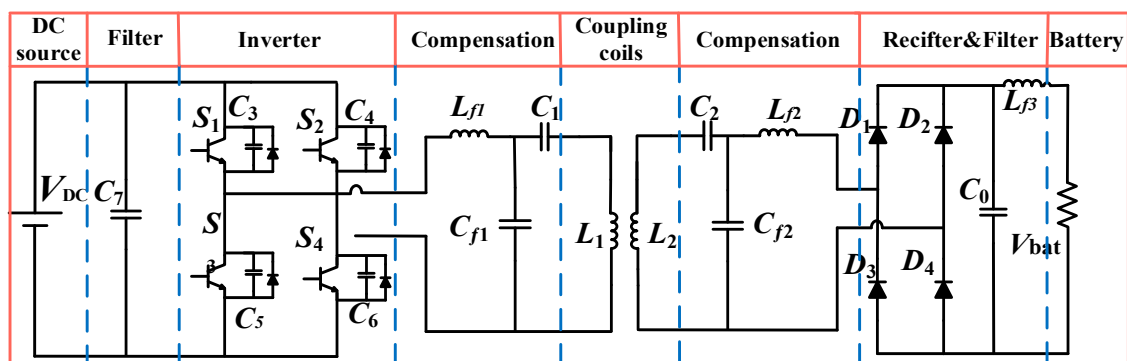


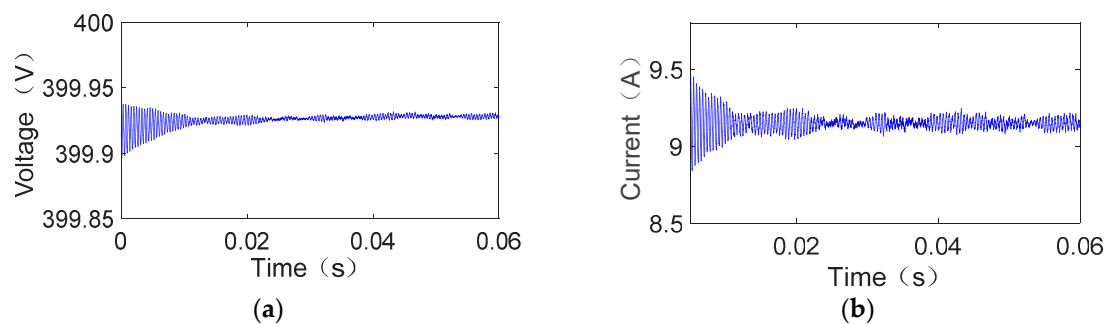
Figure 4. Construction of the WCS.

Table 2. Circuit parameters of wireless charging system (WCS).

Symbol	Meaning	Value
V_{DC}	DC power supply	425 V
L_1, L_2	Inductance of primary coil and secondary coil	226.4 μ H
L_M	Mutual inductance of primary coil and secondary coil	79.8 μ H
C_{f1}, C_{f2}	Primary and secondary compensated capacitor	55.9 nF
L_{f1}, L_{f2}	Primary and secondary compensated inductance	62.7 μ H
C_1, C_2	Primary and secondary compensated capacitor	21.4 nF/24.1 nF
C_0	Rectifier inductance	34.3 μ F
L_{f3}	Rectifier capacitor	131 μ H
V_{bat}	Equivalent resistance	40 Ω

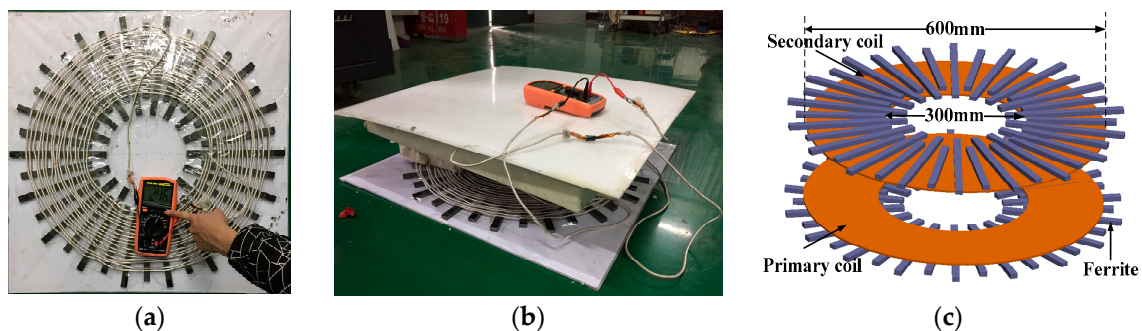
3.2. Simulation of the Electrical Characteristics of WCS

Based on the construction of the WCS in Figure 4, a WCS model is set up in Matlab/Simulink software to obtain the electrical characteristics of the WCS. The inverter circuit is driven by two pairs of sinusoidal pulse width modulation (SPWM) in complementary phase. The voltage and current for the battery are shown in Figure 5, respectively. It can be found that the current is 9.15 A and the voltage is 400 V to meet the 3.7 kW power requirement.

**Figure 5.** WCS functional simulation results (a) Charging current; (b) Charging voltage.

3.3. Parasitic Parameters

The parameters of the power component in WCS can be tested directly, such as when the self-inductance L_1 and L_2 , mutual inductance L_M and distributed capacitance C_{10} of the coils are measured by using the RC meter as shown in Figure 6a,b. Meanwhile, the parameters can also be obtained through modeling and simulation in ANSYS as shown in Figure 6c. The simulation results are in agreement with the measurement results, as shown in Tables 2 and 3.

**Figure 6.** Parameters acquisition (a) Self-inductance; (b) Mutual inductance (c) ANSYS simulation.

From Figure 4, there are some parasitic parameters in inverter system in WCS. Among them, L_{P1} , L_{P2} are inductances of connecting cables, L_P , R_S are the parasitic inductances and parasitic resistance of C_7 , C_3 – C_6 are the inter-electrode inductances of the MOSFET, R_{L0} , R_{L1} , R_{L2} , R_{Lf1} , R_{Lf2} are the parasitic resistances of C_0 , the coupling coils, L_{f1} and L_{f2} , respectively. L_{C0} , L_{Cf1} , L_{Cf2} , L_{C1} and L_{C2} are the parasitic inductances of C_0 , L_{f1} , L_{f2} , C_1 and C_2 , respectively. L_{cable1} , L_{cable2} , L_{cable3} , R_{cable1} , R_{cable2} and R_{cable3} are the parasitic inductances and parasitic resistances on the connecting cable respectively. C_{11} , C_{12} and C_{13} are parasitic capacitances of primary coil, secondary coil and battery relative to the ground; C_{10} is mutual capacitance of the coupling coils. C_{14} , C_{15} are the parasitic capacitances of the two arms midpoint of the inverter relative to the ground.

It is necessary that the parasitic parameters should be extracted and determined for modeling of the WCS for the conducted-EMI. Some measurements for Z parameters and S parameters were made with time-domain reflectometry and a vector network analyzer. A modeling method based on measurement-based model of the electromagnetic emissions is used to achieve high-frequency circuit model for element and system. The value of elements such as inductance or capacitance is regulated and determined by comparing between the simulation and measurement of Z parameters and S parameters [23], as shown in Table 3.

Table 3. Parasitic parameters of WCS.

Symbol	Value	Symbol	Value
L_{P1}, L_{P2}	10 nH	R_{Lf1}, R_{Lf2}	0.03 Ω
L_{C0}	50 nF	R_{Lf3}	1 $\mu\Omega$
L_P	0.2 μ H	R_{L1}/R_{L2}	115 $\mu\Omega$
L_{Cf1}, L_{Cf2}	10 nH	C_{p1}/C_{p2}	380 pF
L_{C1}, L_{C2}	8 nH	C_3 – C_6	142 pF
$L_{cable1}, L_{cable2}, L_{cable3}$	1.76 μ H	C_{10}	21.4 nF
$R_{cable1}, R_{cable2}, R_{cable3}$	0.0524 Ω	C_{11}/C_{12}	80 pF
R_S	0.1 Ω	C_{13}	130 pF

Therefore, an equivalent circuit of the WCS with high-frequency parasitic parameters is built, and the symbol of parasitic parameters is marked by blue color as shown in Figure 7.

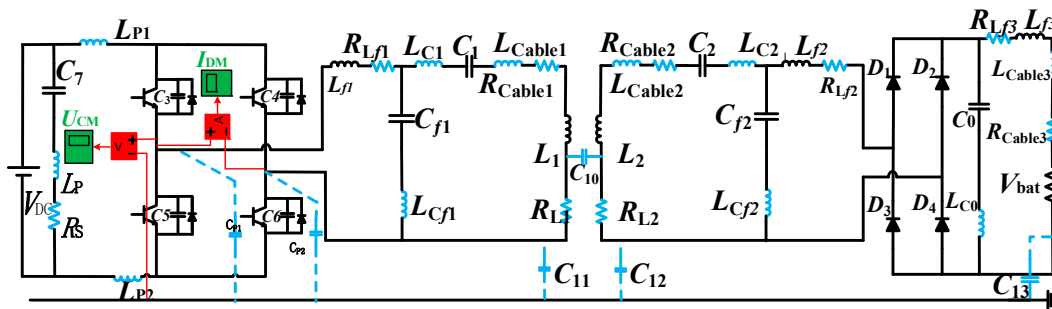


Figure 7. Equivalent circuit for EMI emission.

3.4. Noise Source

Fast switching of the MOSFETs of inverter causes large dv/dt and di/dt , as a result introduces conducted-EMI emissions. Therefore, the interference signal can be extracted from inverter arms. According to Figure 7, a circuit model with high-frequency parameters is built in Matlab/Simulink to obtain the noise source signals of CM interference and DM interference. The red blocks present the sensor of voltage or current, the green blocks present the collector of voltage or current. The noise source signals of CM interference and DM interference are shown in Figure 8, respectively.

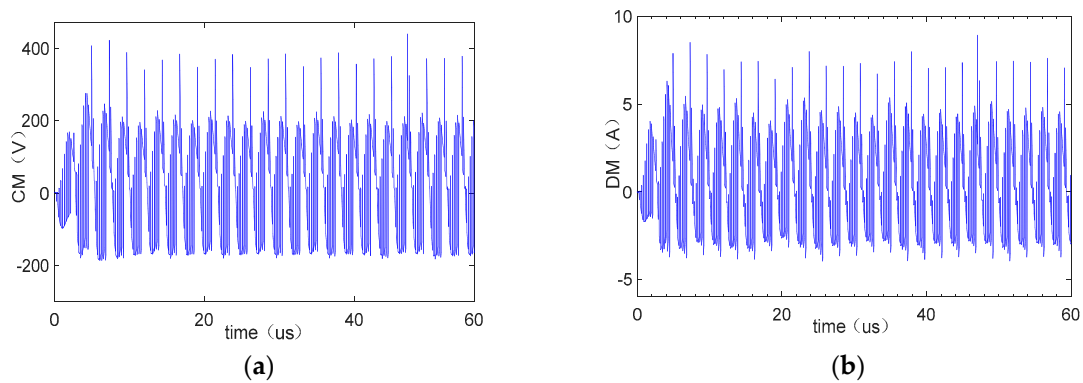


Figure 8. Noise source (a) common mode (CM) source; (b) differential mode (DM) source.

3.5. Modeling and Simulation of the WCS for the Conducted-EMI

Computer Simulation Technology (CST) as an electromagnetic simulation software is used for modeling and simulation for EMC. The conducted and radiated emissions in the wide range frequency and time domains can be obtained by CST. A high-frequency circuit model for the WCS is established by CST to obtain the conducted interference voltage, as shown in Figure 9. The signals of the DM and CM interference sources U_{CM} and I_{DM} are obtained from Matlab/Simulink, as mentioned in Section 3.4. Because conducted interference voltage is an important indicator of conducted-EMI, the model of LISNs consist of R_1 , R_2 , C_8 and C_9 is built to obtain the conducted interference voltage by adding probe P1 and P2.

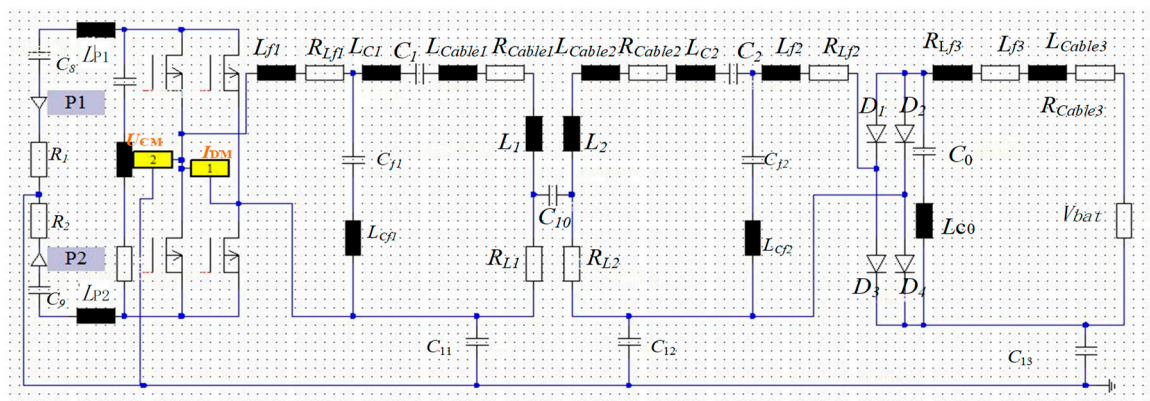


Figure 9. Computer Simulation Technology (CST) model for EMI emission.

The conducted voltage simulation results are compared with the experimental results as shown in Figure 10. It can be found that the conducted voltage characteristics of simulation are basically same as those in the experiment. From Figure 10, it can be shown that the second harmonic appears at 170 kHz, the harmonic frequency interval is 85 kHz in the low frequency band, which is consistent with the switching frequency of MOSFET in inverter of WCS, the resonance phenomenon appears at 30 MHz and the amplitude of conducted voltage is similar before 30 MHz. Meanwhile, the conducted voltage in both cases exceeds CISPR25 (GB/T18655-2010) limits in the frequencies range of 500 kHz–2 MHz and 25 MHz–30 MHz. So in the frequencies range of 150 kHz–30 MHz, the high-frequency equivalent circuit of the WCS established by CST has a high accuracy in somehow. However, there is some difference between simulation and experiment results in the frequencies range of 30 MHz–108 MHz. Because some high-frequency parasitic parameters in the frequencies range of 30 MHz–108 MHz were not taken into consideration.

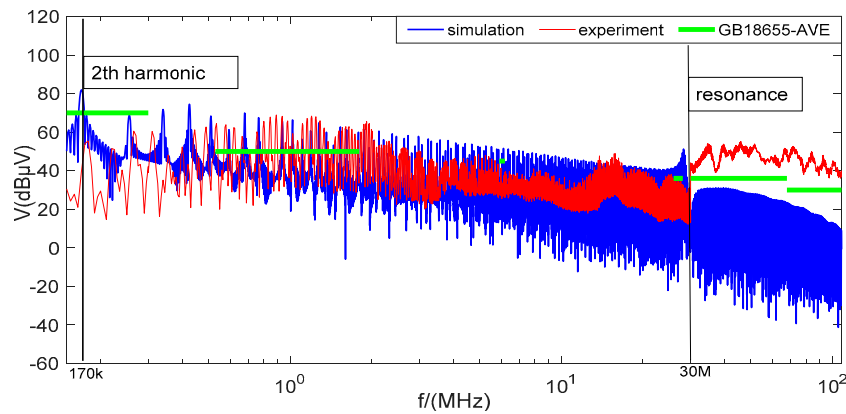


Figure 10. Comparison of simulation and experiment.

4. Analysis and Estimation for the Conducted-EMI

The DM propagation paths and the CM propagation paths for conducted-EMI emission model of the WCS are respectively carried out. The following simulations are based on the assumption that the S_1 and S_4 are conducting, S_2 and S_3 are non-conducting and the current flows through C_4 and C_5 . The sources of the noises are injected at midpoint of the first arm due to the symmetry of the circuit.

4.1. Analysis for DM Propagation Paths

There is a parasitic capacitor C_{10} between primary coil and secondary coil, so the DM interference current may exist in the secondary circuit. However, it depends on the bandwidth of high frequency transformer. This paper focus on the frequency range of 150 kHz–108 MHz, due to the larger capacitive reactance, we assume that the DM interference current mainly exists in the primary circuit. The DM propagation paths of the WCS are shown in Figure 11. The sequence in which the I_{DM} flows through the components is as follows:

- Current loop I_1 : $I_{DM} \rightarrow C_5 \rightarrow L_{P2} \rightarrow \left(\begin{matrix} R_2 \rightarrow C_9 \rightarrow C_8 \rightarrow R_1 \\ R_5 \rightarrow L_P \rightarrow C_9 \end{matrix} \right) \rightarrow L_{P1} \rightarrow I_{DM}$.
- Current loop I_2 :
 $I_{DM} \rightarrow L_{f1} \rightarrow R_{Lf1} \rightarrow \left(\begin{matrix} L_{C1} \rightarrow C_1 \rightarrow L_{Cable1} \rightarrow R_{Cable1} \rightarrow L_1 \rightarrow R_{L1} \\ R_5 \rightarrow L_P \rightarrow C_9 \end{matrix} \right) \rightarrow L_{P2} \rightarrow \left(\begin{matrix} R_2 \rightarrow C_9 \rightarrow C_8 \rightarrow R_1 \\ R_5 \rightarrow L_P \rightarrow C_7 \end{matrix} \right) \rightarrow L_{P1} \rightarrow I_{DM}$.

From Figure 11, it can be seen that the DM interference current passes through the LISNs and the power cables which connects with the DC voltage source. So it is possible that the DM interference current may not only flow on the DC power cables but can also affect the quality of the DC voltage source.

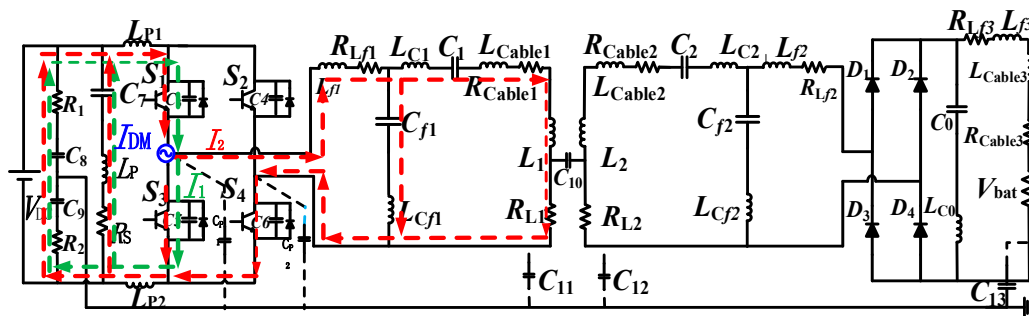


Figure 11. Analysis for DM interference: DM current path.

The equivalent circuit of the DM interference paths is shown in Figure 12. From Figure 12, it can be seen that Z_1 , Z_2 , Z_3 , Z_4 and Z_5 represent part of circuit impedance, respectively. And the function was given by Equations (1)–(5). The relationship between the output noise energy and the input noise energy in the system is given by the transfer function in Equation (6). Then, a Bode-diagram for the transfer function is drawn, as shown in Figure 13. From (6) and Figure 13, some DM interference elements in the frequencies range of 150 kHz–180 MHz can be illustrated.

$$Z_1 = R_1 + \frac{1}{sC_8} + \frac{1}{sC_9} + R_2 \quad (1)$$

$$Z_2 = \frac{1}{sC_7} + sL_P + R_S \quad (2)$$

$$Z_3 = sL_{f1} + R_{Lf1} + \frac{1}{sC_1} \quad (3)$$

$$Z_4 = sL_{cf1} + \frac{1}{sC_{f1}} \quad (4)$$

$$Z_5 = \frac{1}{sC_1} + sL_{cable1} + R_{cable1} + sL_1 + R_{L1} \quad (5)$$

$$G(S_1) = \frac{V_{RD}}{V_{DM}} = \frac{Z_1 // Z_2}{(Z_1 // Z_2) + [Z_3 + (Z_4 // Z_5)] // C_3 + Z_{LP1} + Z_{LP2}} \cdot \frac{Z_{R1}}{Z_1} \quad (6)$$

$$= \frac{3.75e^{-32}s^4 + 7.5e^{-26}s^3 + 3.875e^{-20}s^2 + 2.5e^{-15}s^5 + 1.25e^{-9}}{2.25e^{-63}s^9 + 6.75e^{-57}s^8 + 2.255e^{-48}s^7 + 6.75e^{-42}s^6 + 6.9e^{-36}s^5 + 2.7e^{-30}s^4 + 4.525e^{-25}s^3 + 1.575e^{-19}s^2}}$$

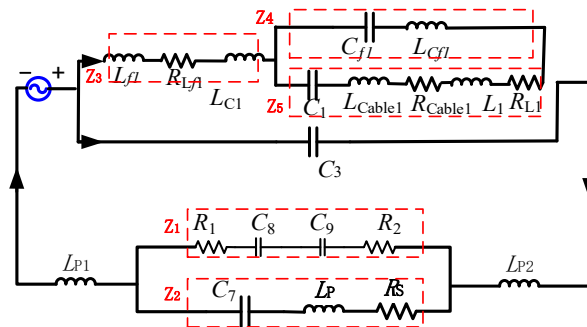


Figure 12. Analysis for DM interference: Equivalent circuit diagram.

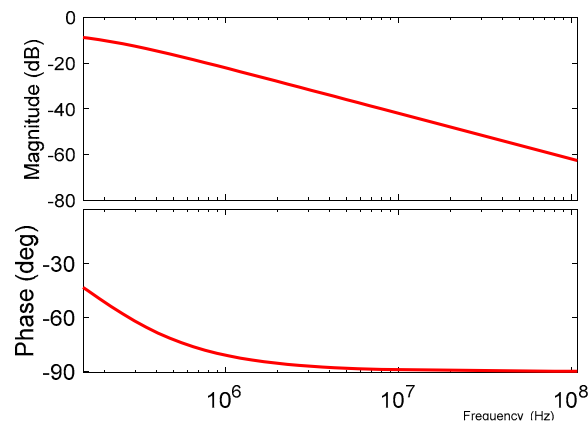


Figure 13. Bode-diagram for DM interference.

From Figure 13, it can be also seen that the DM conducted voltage is -10 dB μ V at 150 kHz. Along with the frequency increasing, the magnitude of the DM conducted interference voltage is rapidly declining. Thus, the DM interference mainly exists at the low frequency band.

4.2. Analysis for CM Propagation Paths

Similarly, there are four different CM propagation paths as shown in Figure 14, it can be found that the CM interference current passes the LISNs and the power cables connected to the DC voltage source. The sequence in which the I_{CM} flows through the components is as follows:

- Current loop I1: $I_{CM} \rightarrow \left(\begin{smallmatrix} C_5 \rightarrow L_{P2} \rightarrow R_2 \rightarrow C_9 \\ L_{P1} \rightarrow R_1 \rightarrow C_8 \end{smallmatrix} \right) \rightarrow \text{ground} \rightarrow I_{CM}$;
- Current loop I2: $I_{CM} \rightarrow \left(\begin{smallmatrix} E_1 \rightarrow R_{L1} \\ C_5 \end{smallmatrix} \right) \rightarrow C_{11} \rightarrow \text{ground} \rightarrow I_{CM}$;
- Current loop I3: $I_{CM} \rightarrow E_1 \rightarrow C_{10} \rightarrow \left(\begin{smallmatrix} E_2 \rightarrow E_3 \rightarrow V_{bat} \rightarrow C_{13} \\ R_{12} \rightarrow C_{12} \end{smallmatrix} \right) \rightarrow \text{ground} \rightarrow I_{CM}$;
- Current loop I4: $I_{CM} \rightarrow C_{P1} \rightarrow \text{ground} \rightarrow I_{CM}$.

Among them, E_1 is a path of $L_{f1} \rightarrow R_{Lf1} \rightarrow L_{C1} \rightarrow C_1 \rightarrow L_{cable1} \rightarrow R_{cable1} \rightarrow L_1$; E_2 is a path of $L_2 \rightarrow L_{cable2} \rightarrow R_{cable2} \rightarrow C_2 \rightarrow L_{C2} \rightarrow L_{f2} \rightarrow R_{Lf2}$ and E_3 is a path of $R_{Lf3} \rightarrow L_{f3} \rightarrow L_{cable3} \rightarrow R_{cable3}$.

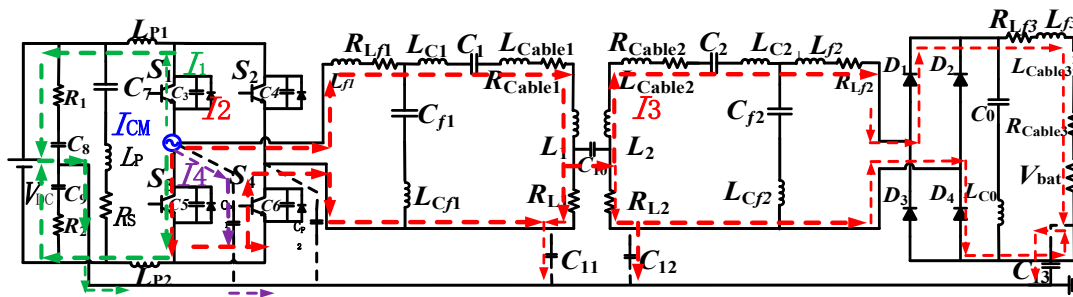


Figure 14. Analysis for CM interference: EMI current path.

This part of the interference current may generate conducted-EMI from DC power cables at ground side and battery side in EVs, so it is significant to predict the CM interference of WCS. An equivalent circuit of the CM interference paths is shown in Figure 15, R_{L2} and L_2 are divided equally into $RL2-1$, $RL2-2$ and $L2-1$, $L2-2$. In Figure 15, you can see Z_1 , Z_2 , Z_3 , Z_4 and Z_5 and Z_6 which represent a part of circuit impedance, respectively. And the function was established by Equations (7)–(12). The relationship between the output noise energy and the input noise energy in the system is given by transfer function in Equation (13). Then, the bode-diagram of the transfer function is drawn, as shown in Figure 16. From Equation (13) and Figure 16, some CM interference elements in the frequencies range of 150 kHz–180 MHz can be illustrated.

$$Z_1 = (R_1 + \frac{1}{sC_8} + sL_{P1}) // (sL_{P2} + \frac{1}{sC_9} + R_2 + \frac{1}{sC_5}) \quad (7)$$

$$Z_2 = sL_{2-2} + R_{2-2} + R_{bat} \quad (8)$$

$$Z_3 = sL_{2-1} + R_{2-1} + sL_{cable2} + R_{cable2} + sL_{f2} + R_{Lf2} + sL_0 + R_{L0} + \frac{1}{sC_2} + sL_{C2} + sL_{cable3} + R_{cable3} \quad (9)$$

$$Z_4 = sL_{cf1} + R_{Lf1} + sL_{C1} + \frac{1}{sC_1} + sL_{cable1} + R_{cable1} + sL_{C1} + R_{L1} \quad (10)$$

$$Z_5 = (Z_2 // Z_3) + Z_{C13} \quad (11)$$

$$Z_6 = [(Z_5 + Z_4) // Z_{C5}] + Z_{C11} \quad (12)$$

$$\begin{aligned}
 G(S_2) &= \frac{V_{RC}}{V_{CM}} = \frac{(Z_6 // Z_{CP1}) R_1}{(Z_1 // Z_6 // Z_{CP1})^2 (Z_{CP1} + Z_{C8} + R_1)} \\
 &= \frac{7.32e^{-3}s^4 + 2.446e^5s^3 + 2.078e^{10}s^2 + 4.4418e^{14}s^5}{7.294e^4s^7 + 1.23e^{12}s^6 + 1.56e^{17}s^5 + 6.631e^{21}s^4 + 9.4e^{25}s^3}
 \end{aligned} \quad (13)$$

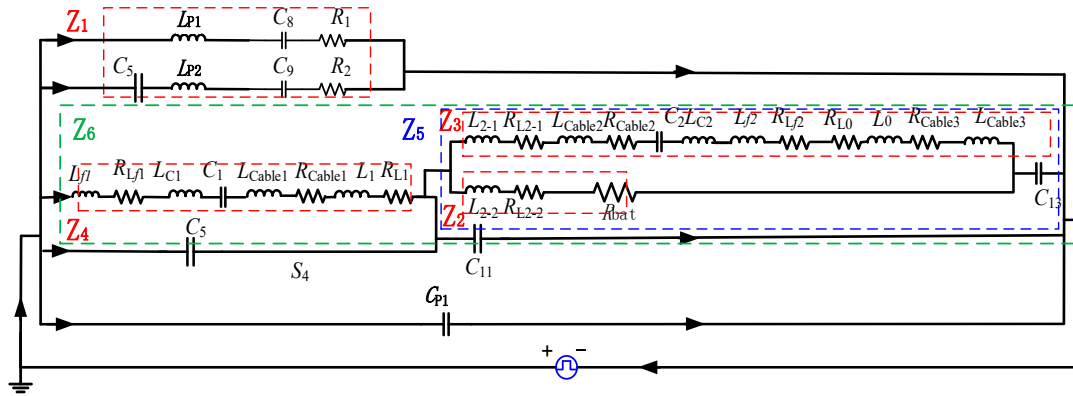


Figure 15. Analysis for CM interference: Equivalent circuit diagram.

It can be seen that the magnitude of the CM interference voltage is between $-5 \text{ dB}\mu\text{V}$ and $0 \text{ dB}\mu\text{V}$ in the frequency range of 150 kHz – 108 MHz , which is much higher than DM interference.

In summary, from the view of Bode diagram and transfer function, it can be seen that the DM interference is not obvious and decreases along with the increase of frequency. The CM interference exists in all frequency bands and the magnitude of interference is relatively higher. Therefore, the CM interference has a great influence for the conducted interference of the WCS.

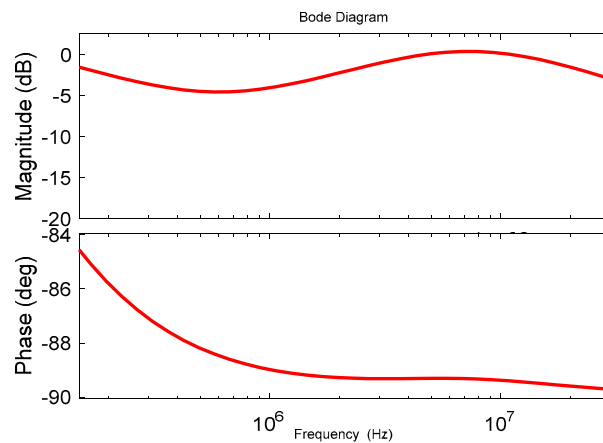


Figure 16. Bode diagram for CM interference.

4.3. Simulation Results for CM and DM Conducted Voltage

The conducted interference measured by LISNs appears as conducted voltage. And the comparison between the one mode and CM+DM conducted voltage are shown in Figure 17. The black curve represents the conducted voltage of the CM+DM mode simulation, the red curve represents the DM conducted voltage and the blue curve represents the CM conducted voltage. It can be seen that some resonances appear at the same frequency 170 kHz , 430 kHz , 1.6 MHz , 30 MHz and the amplitude of those resonances are similar in the CM+DM waveform and CM waveform. However, in all frequency bands, the DM conducted voltage is smaller than that in CM+DM, especially at 30 – 108 MHz . Meanwhile the resonance point is shifted. Thus, from the view of conducted voltage, the CM waveform of the conducted voltage are better to represent the CM+DM waveform in fact.

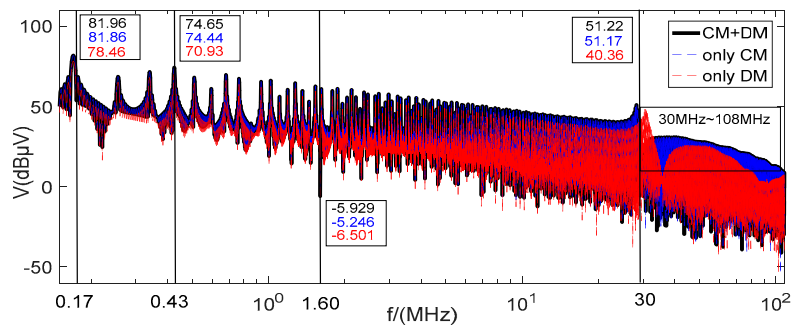


Figure 17. The conducted voltage measured on line impedance stabilization networks (LISNs).

The simulation result of the conducted voltage is consistent with the change of the transfer function by bode diagram. Therefore, from Figures 16 and 17, it can be concluded that the CM interference is mainly responsible for the conducted-EMI from the DC power cables of WCS.

5. Filters Design and Experiments

The passive filter design method is used to determine the values of the major components in the EMI filter. From above discussion, the conducted interference of the WCS comes mainly from CM interference. Therefore, giving priority to designing the CM filter is taken into account to mitigate the conducted-EMI in WCS in EVs. Then, designing DM filter is considered if necessary.

5.1. Calculating Parameters in EMI Filters

The first step is to determine required filter attenuation for CM conducted-EMI and the CM conducted voltage in blue curve as shown in Figure 18. The CM attenuation A_{CM} is calculated by the Equation (14):

$$A_{CM} = A_{nCM} - A_{ST} + m \quad (14)$$

here, A_{nCM} is amplitude of the maximum conducted voltage; A_{ST} is the limits of standard CISPR25 (GB/T 18655-AVE) level 3; m is the safety margin (6 dBμV).

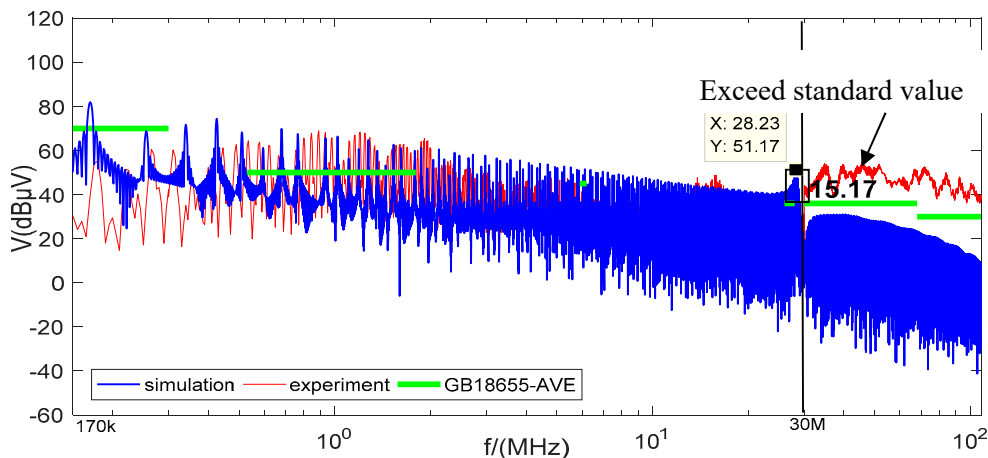


Figure 18. Simulation results for CM conducted voltage.

It can be seen from Figure 18, the conducted voltage obtained from the experimental all meet the standard limit in the frequency range of 150 kHz–500 kHz and partially meet standard in the frequencies range of 500 kHz–2 MHz. However, it all exceeded standard in the frequencies range of 30 MHz–108 MHz. Among them, the maximum conducted voltage appears at 30 MHz. Therefore,

the frequency point at 30 MHz is selected as a target attenuation frequency and expressed as f_{aim} . The conducted voltage at 30 MHz is 51.17 dB μ V and the A_{ST} is 36 dB μ V. So, the target attenuation of CM conducted interference can be obtained as $A_{CM} = 51.17 - 36 + 6 = 21.17$ dB μ V.

The second step is to specify the filter corner frequency. It is determined by the target attenuation frequency. Thus, the corner frequency can be specified by the Equation (15):

$$f_0 = \frac{f_{aim}}{10^{\frac{A_{CM}}{S}}} \quad (15)$$

where, S is the slope rate of the decay ramp of 40 dB/dec. So the f_0 is equal to 54.55 MHz.

The CM inductance L_C and CM capacitance C_Y can be calculated by Equation (16):

$$L_C = \left(\frac{1}{2\pi f_0} \right)^2 \times \frac{1}{2C_Y} \quad (16)$$

Obviously, there is much possibility for the combination of L_C and C_Y . According to Equation (16), it can be seen that C_Y and L_C are inversely proportional to each other. Generally, assuming that the constant value of C_Y is 500 nF, the value of L_C can be calculated as 265 μ H. The filter series connected between LISNs and WCS as shown in Figure 19.

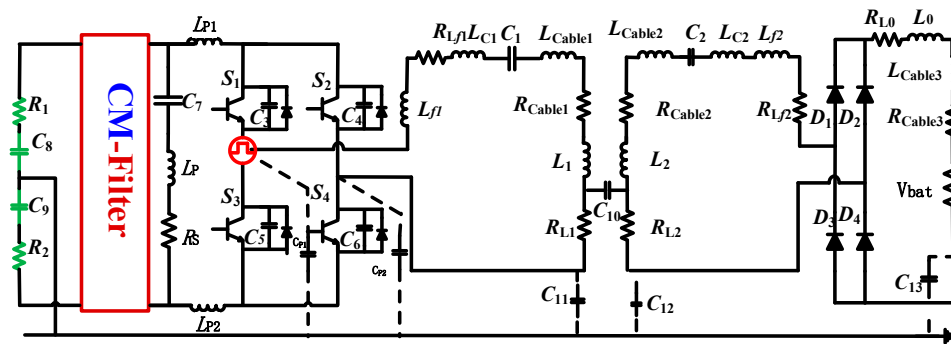


Figure 19. WCS circuit with the CM filter.

5.2. Topology Selection of CM Filter

In order to select the best filter topology with considering the volume and weight of the filter, CL, LC and CLC topology are designed and modeled in CST. The conducted voltage of simulation results with three types filters are shown in Figure 20.

In Figure 20, the conducted voltages of different topology circuits with LC, CLC and CL are displayed by three colors. There are some harmonic in the low-frequency bands, the value of the conducted voltages of Nth harmonic (2th = 170 kHz, 3th = 255 kHz, 4th = 340 kHz, 5th = 425 kHz) and 1 MHz are listed in Table 4. It is obvious that the smallest value of conducted voltage and harmonic content appears in the circuit with CL filter. The conducted voltage by using LC filter is good after 2 MHz, but it causes a new resonance and still exceeds the standard at 1 MHz. Although the mitigation of the conducted voltage by using CLC filter is also well, the cost and volume of the CLC are larger than others. Therefore, the CL topology is the best choice for CM filter due to the best suppression, the smallest number of components, the smallest volume and weight, compared with LC and CLC topology.

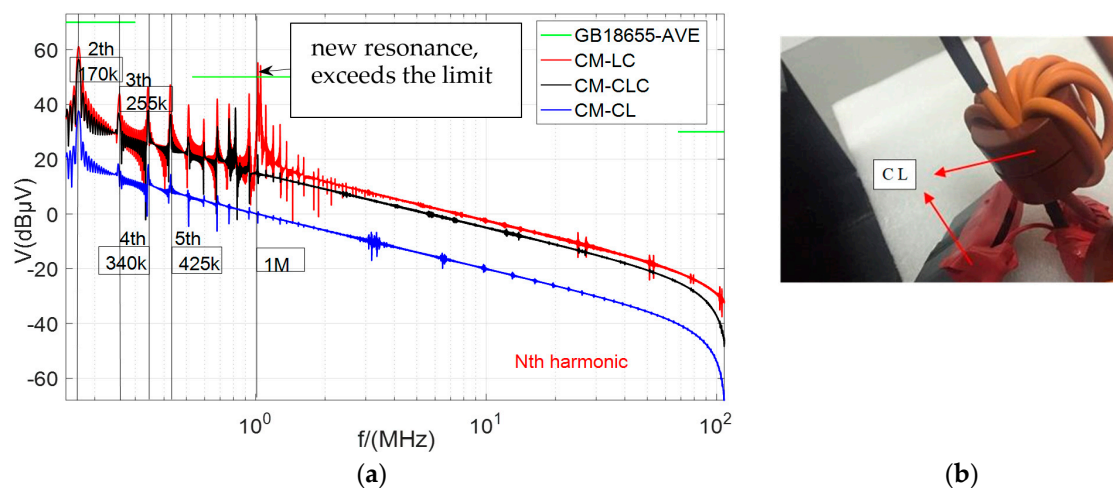


Figure 20. EMI filters (a) Comparison of different topologies; (b) Designed CL filter.

From Figure 20, by adding the CL topology CM filter, the conducted voltage in the frequency 150 kHz–108 MHz can be decreased to below the limits of standard GB/T 18655-AVE level 3 and the harmonic wave is obviously suppressed. In addition, it is unnecessary to design DM filters.

Table 4. The value of conducted voltage in three circuits of WCS.

Circuit with Filter	Value of Conducted Voltage (dBμV)					Characteristic
	170 kHz	255 kHz	340 kHz	425 kHz	1 MHz	
LC filter	61.12	43.91	43.91	47.14	55.18	With new resonance, fewer components
CLC filter	56.48	36.86	37.83	36.32	24.70	Good mitigation, more components and volume
CL filter	38.57	18.26	18.03	14.43	6.36	Better mitigation, fewer components

6. Experimental Verification

6.1. Electrical Experiment of WCS in EVs

An experimental system is built to validate the rightness and feasibility of the proposed design method, as shown in Figure 21. Figure 21a shows a wireless charging system with power of 3.7 kW. The secondary charging coil is installed on the chassis, and the primary charging coil is installed under the ground. The WCS transfer power to the battery. Figure 21b shows the visual information on the instrument panel when the electric vehicle is charging. From Figure 21b, the voltage and current of fast charging are 400 V and 9 A, in addition, the outside temperature is -3°C , and the mileage for current power reaches 148 km, so the WCS that we built can achieve the charge normally.

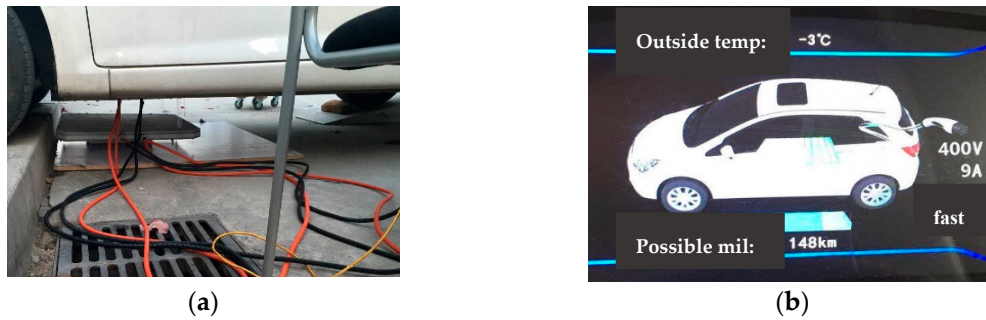


Figure 21. WCS experiment (a) Coupling coils; (b) Dashboard Information.

6.2. Conducted Emission Experiments

A conducted emission experiments is setup when the WCS is working. Then, a CL filter is added in the WCS which is shown in Figure 2, so as to validate the attenuation effect of the conducted emission from DC-fed WCS. According to the filter structure designed in Section 5, the CL topology CM filter is added at DC input terminals inside of the controller. Then, Figure 22 shows the conducted voltage on the primary DC power cable after adding the CL filter. From Figure 22, the mitigation of the conducted voltage in low frequency band is obvious, the conducted voltage is lower than the limit of CISPR 25 (GB/T18655) in all frequency bands, as result in meeting the standard requirements.

The conducted voltage measured in the experiment without filter is A_{e1} , after adding the CL filter, the conducted voltage is A_{e2} , and the actual attenuation at 30 MHz can be expressed as Equation (17):

$$A_{e1} - A_{e2} = 43.6 - 22.2 = 21.4 \text{ dB}\mu\text{V} \quad (17)$$

At 30 MHz, the expected attenuation for CM filter with CL topology is 21.17 dB μ V, and the experimental attenuation is 21.4 dB μ V, from which a good consistence is achieved. It means that the mitigation of the proposed CM filter with CL topology is accurate, and shows the effectiveness and feasibility of only adding the CM filter as well. From the experiments results in Figure 22, based on giving priority for designing CM filter, the mitigation conducted emission strategy is suitable and feasible.

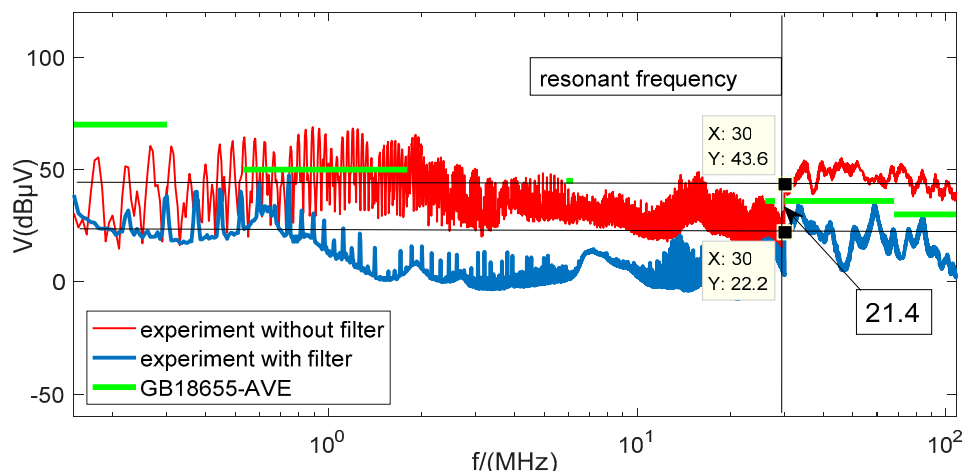


Figure 22. Comparison of experiments results.

7. Conclusions

A mitigation conducted emission strategy based on transfer function from a DC-fed WCS for EVs is proposed. An equivalent circuit model with high-frequency parasitic parameters for the DC-fed

WCS for EVs is built based on measurement. The characteristics of conducted emission from DC power cables is obtained in a frequency range of 150 kHz–108 MHz by measurement and simulation. The transfer functions of DM interference and CM interference were established. A judgment method of using transfer functions to determine the dominated interference mode responsible for EMI is proposed. Compared with the simulation results of the mitigation of DM interference, it can be seen that the CM interference is the dominated interference mode and responsible for the conducted EMI from DC power cables of the WCS. A strategy of giving priority to the dominated interference mode is proposed for designing the CM interference filter. The conducted voltage of simulation and experiment is decreased respectively by 21.17 dB μ V and 21.4 dB μ V at resonance frequency 30 MHz. By adding the CL topology CM filter, the conducted voltage in the frequency 150 kHz–108 MHz can be decreased to below the limits of standard CISPR25 (GB/T 18655-AVE) level 3. In the future, the equivalent circuit model for the DC-fed WCS should be improved in the frequency 30 MHz–108 MHz.

Acknowledgments: This paper was supported by the National Natural Science Foundation of China for financially supporting this project (51475045).

Author Contributions: Li Zhai and Yu Cao designed the methodology and wrote the manuscript. Liwen Lin and Tao Zhang conceived and design the experiments. Steven Kavuma implemented the experiments. All authors contributed improving the quality of the manuscript.

Conflicts of Interest: The authors declare no conflict of interest.

References

1. Lee, W.; Hong, Y.K.; Park, J.H.; Lee, J. A simple wireless power charging antenna system: Evaluation of ferrite sheet. *IEEE Trans. Magn.* **2017**, *53*. [[CrossRef](#)]
2. Ho, S.L.; Wang, J.; Fu, W.N. A comparative study between novel witricity and traditional inductive magnetic coupling in WPT. *IEEE Trans. Magn.* **2011**, *47*, 1522–1525. [[CrossRef](#)]
3. Soo, I.S. *WPT Technology and the Future of Electric Transportation*; SAE International: Warrendale, PA, USA, 2015.
4. Lee, S.B.; Ahn, S.; Jang, I.G. Development of the optimization framework for low-power wireless power transfer systems. *IEEE Trans. Microw. Theory Tech.* **2015**, *63*, 813–820. [[CrossRef](#)]
5. Xiao, C.; Wei, K.; Cheng, D.; Liu, Y. Wireless charging system considering eddy current in cardiac pacemaker shell: Theoretical modeling, experiments, and safety simulations. *IEEE Trans. Ind. Electron.* **2017**, *64*, 3978–3988. [[CrossRef](#)]
6. Wang, W.; Hemour, S.; Wu, K. Coupled Resonance Energy Transfer Over Gigahertz Frequency Range Using Ceramic Filled Cavity for Medical Implanted Sensors. *IEEE Trans. Microw. Theory Tech.* **2014**, *62*, 956–964. [[CrossRef](#)]
7. Lu, Y.; Ma, D. Wireless Power Transfer System Architectures for Portable or Implantable Applications. *Energies* **2016**, *9*, 1087. [[CrossRef](#)]
8. Chen, W.; Liu, C.; Lee, C.; Shan, Z. Cost-Effectiveness Comparison of Coupler Designs of Wireless Power Transfer for Electric Vehicle Dynamic Charging. *Energies* **2016**, *9*, 906. [[CrossRef](#)]
9. Esteban, B.; Sid-Ahmed, M.; Kar, N. A Comparative Study of Power Supply Architectures in Wireless EV Charging Systems. *IEEE Trans. Power Electron.* **2015**, *30*, 6408–6422. [[CrossRef](#)]
10. Rozman, M.; Fernando, M. Combination of Compensations and Multi-Parameter Coil for Efficiency Optimization of Inductive Power Transfer System. *Energies* **2017**, *10*, 2088.
11. Geng, Y.; Li, B.; Yang, Z. A High Efficiency Charging Strategy for a Supercapacitor Using a Wireless Power Transfer System Based on LCC Compensation Topology. *Energies* **2017**, *10*, 135. [[CrossRef](#)]
12. Xiao, C.Y.; Liu, Y.F. New Insight of Maximum Transferred Power by Matching Capacitance of a Wireless Power Transfer System. *Energies* **2017**, *10*, 688. [[CrossRef](#)]
13. Dai, X.; Li, Y.; Li, X.; Deng, P.; Tang, C. A Maximum Power Transfer Tracking Method for Wireless charging systems with Coupling Coefficient Identification Considering Two-Value Problem. *Energies* **2017**, *10*, 1665. [[CrossRef](#)]
14. Zeng, H.; Liu, Z.; Hou, Y.; Tong, H.; Zhou, B. Optimization of magnetic core structure for WPT coupler. *IEEE Trans. Magn.* **2017**, *53*, 1. [[CrossRef](#)]

15. Mahmoud, H.; Elmahmoud, W. Efficient wireless power charging of electric vehicle by modifying the magnetic characteristics of the transmitting medium. *IEEE Trans. Magn.* **2017**, *53*, 1. [[CrossRef](#)]
16. Moon, H.; Kim, S.; Park, H.H. Design of a resonant reactive shield with double coils and a phase shifter for WPT of electric vehicles. *IEEE Trans. Magn.* **2015**, *51*, 1–4. [[CrossRef](#)]
17. Hui, S.Y.R.; Zhong, W.; Lee, C.K. A Critical Review of Recent Progress in Mid-Range Wireless Power Transfer. *IEEE Trans. Power Electron.* **2014**, *29*, 4500–4511. [[CrossRef](#)]
18. Piazza, M.C.D.; Giglia, G. EMI filter design in motor drives with Common Mode voltage active compensation. In Proceedings of the 2014 IEEE 23rd International Symposium on Industrial Electronics (ISIE), Istanbul, Turkey, 1–4 June 2014; pp. 800–805.
19. Zhai, L.; Lin, L.; Zhang, X. The Effect of Distributed Parameters on Conducted EMI from DC-Fed Motor Drive Systems in Electric Vehicles. *Energies* **2016**, *10*, 1. [[CrossRef](#)]
20. Ala, G.; Giaconia, G.; Giglia, G. Design and performance evaluation of a high power density EMI filter for PWM inverter-fed induction motor drives. *IEEE Trans. Ind. Appl.* **2016**, *52*, 1573–1579. [[CrossRef](#)]
21. Zhai, Li.; Zhang, X.; Bondarenko, N. Mitigation Emission Strategy Based on Resonances from a Power Inverter System in Electric Vehicles. *Energies* **2016**, *9*, 419. [[CrossRef](#)]
22. Sun, J.; Chen, W.; Yang, X. EMI prediction and filter design for MHz GaN based LLC half-bridge converter. In Proceedings of the 2016 IEEE 8th International Power Electronics and Motion Control Conference, Hefei, China, 22–26 May 2016; pp. 297–304.
23. Bondarenko, N.; Zhai, L.; Xu, B. A Measurement-Based Model of the Electromagnetic Emissions from a Power Inverter. *IEEE Trans. Power Electron.* **2015**, *30*, 5522–5531. [[CrossRef](#)]



© 2018 by the authors. Licensee MDPI, Basel, Switzerland. This article is an open access article distributed under the terms and conditions of the Creative Commons Attribution (CC BY) license (<http://creativecommons.org/licenses/by/4.0/>).